PHYSICAL REVIEW MATERIALS **1**, 073603 (2017)

Electronic properties of doped and defective NiO: A quantum Monte Carlo study

Hyeondeok Shin[*]
Argonne Leadership Computing Facility, Argonne National Laboratory, Lemont, Illinois 60439, USA

Ye Luo
Argonne Leadership Computing Facility, Argonne National Laboratory, Lemont, Illinois 60439, USA

Panchapakesan Ganesh
Center for Nanophase Materials Sciences Division, Oak Ridge National Laboratory, Oak Ridge, Tennessee 37831, USA

Janakiraman Balachandran
Center for Nanophase Materials Sciences Division, Oak Ridge National Laboratory, Oak Ridge, Teneessee 37831, USA

Jaron T. Krogel
Material Science and Technology Division, Oak Ridge National Laboratory, Oak Ridge, Tennessee 37831, USA

Paul R. C. Kent
Center for Nanophase Materials Sciences and Computational Science and Engineering Division,
Oak Ridge National Laboratory, Oak Ridge, Tennessee 37831, USA

Anouar Benali
Argonne Leadership Computing Facility, Argonne National Laboratory, Lemont, Illinois 60439, USA

Olle Heinonen[†]
Material Science Division, Argonne National Laboratory, Argonne, Illinois 60439, USA
and Northwestern-Argonne Institute for Science and Engineering, 2205 Tech Drive, Suite 1160, Evanston, Illinois 60208, USA

(Received 29 August 2017; revised manuscript received 28 November 2017; published 28 December 2017)

NiO is a canonical Mott (or charge-transfer) insulator and, as such, is notoriously difficult to describe using density functional theory (DFT)–based electronic structure methods. *Doped* Mott insulators such as NiO are of interest for various applications but rigorous theoretical descriptions are lacking. Here, we use quantum Monte Carlo methods, which very accurately include electron-electron interactions, to examine energetics, charge structures, and spin structures of NiO with various point defects, such as vacancies and substitutional doping with potassium. The formation energy of a potassium dopant is significantly lower than that of a Ni vacancy, making potassium an attractive monovalent dopant for NiO. We compare our results with DFT results that include an on-site Hubbard U (DFT + U) to account for correlations and find relatively large discrepancies for defect formation energies as well as for charge and spin redistributions in the presence of point defects. Beyond fitting to a single property, it is unlikely that single-parameter tuning of the DFT + U will be able to obtain accurate accounts of complex properties in these materials. Responses that depend in subtle and complex ways on ground-state properties, such as charge and spin densities, are likely to contain quantitative and qualitative errors.

DOI: 10.1103/PhysRevMaterials.1.073603

I. INTRODUCTION

One of the outstanding problems in condensed matter physics is understanding the behavior of systems with strong electronic correlations. By “strong” we refer to correlations strong enough that standard theoretical and modeling techniques, such as noninteracting electrons and standard density-functional-based theories, are inadequate to fully describe the system and yield substantially incorrect results when applied. Strongly correlated systems include, for example, fractional quantum Hall systems, heavy fermions, and Kondo systems but also a large number of transition metal oxides (TMOs) with partially filled $3d$ or $4d$ states. Of the $3d$ TMOs, NiO is a well-studied canonical example of a Mott insulator: strong correlations between the localized $3d$ orbitals in the rock-salt structure drive the ground state of the system to an insulating type II antiferromagnet, rather than a nonmagnetic metal, with parallel spins in the Ni (111) planes and antiferromagnetic coupling between successive Ni (111) planes. NiO has traditionally been considered a classic wide-band-gap Mott insulator [1], while later works have argued that NiO is a p-d charge transfer insulator [2–5]. More generally, NiO has been thought to possess an electronic structure intermediate between that of Mott insulators and that of p-d charge transfer insulators [6,7].

---

[*] hshin@anl.gov

[†] heinonen@anl.gov

Not only is NiO interesting from the perspective of a Mott or charge transfer insulator, but it is typically a p-type semiconductor, one of a very small number of p-type oxides, because as-deposited NiO typically has a Ni deficiency. As a p-type hole-doped oxide, it is interesting from a number of applications, ranging from transparent conducting oxides [8–11] to use in oxide electronics. Pristine stoichiometric NiO consists of Ni^{+2} and O^{-2} ions. Hole states can be generated and populated by increasing the concentration of Ni^{+3} ions by adding defects, such as Ni vacancies and monovalent dopants [12]. Lithium is a well-known monovalent substitutional dopant, and Li-doped NiO ($\mathrm{Li}_x\mathrm{Ni}_{1-x}\mathrm{O}$) has been studied intensively both experimentally and theoretically, with the goal of determining its electronic and optical properties as an enhanced p-type transparent conducting oxide [13–19]. Measurements on $\mathrm{Li}_x\mathrm{Ni}_{1-x}\mathrm{O}$ grown by pulsed laser deposition revealed that the resistivity of Li-doped NiO decreases monotonically to as low as 0.15 Ω-cm at room temperature with increasing Li concentration [20]. However, Li-doped NiO exhibits its minimum resistivity for a very low Li dopant concentration ($x = 0.07$). This makes Li-doped NiO challenging to model using first-principle methods, whether density functional theory (DFT) [16,18,21] or many-body approaches, as a large unit cell is required, or some other method employed to incorporate a low Li concentration.

Potassium has been proposed more recently as a candidate monovalent dopant for NiO. Measurements on K-doped NiO grown by pulsed laser deposition indicate that the minimum room-temperature resistivity of K-doped NiO is about 0.24 Ω-cm for $\mathrm{K}_{0.25}\mathrm{Ni}_{0.75}\mathrm{O}$: a concentration that is significantly higher than the reported Li concentration at minimum resistivity, $\mathrm{Li}_{0.07}\mathrm{Ni}_{0.93}\mathrm{O}$ [22]. Although the minimum resistivity of K-doped NiO was measured to be slightly higher than that of Li-doped NiO, its minimum value is considerably lower than reported values of the resistivity of NiO systems doped with other monovalent dopants, such as sodium [23]. Because of the lack of theoretical information about the electronic properties in NiO systems with substitutional dopants heavier than Li, e.g., K, it is not possible to make meaningful comparisons between point defect energetics, spin density, and other electronic properties of interest, in K-doped and Li-doped NiO. From a more general perspective, these properties in the presence of doping touch on a fundamental question in the field of strongly correlated systems: How do the electronic properties of a Mott insulator evolve upon doping? This is expected to be fundamentally different from doping standard semiconductors such as Si and GaAs, in which the electron-electron interactions are relatively weak and the electronic structure is mean-field-like. As a consequence, the band structures of such semiconductors remain rigid as defect levels are added upon doping. In contrast, the entire electronic structure of a Mott insulator is expected to evolve upon doping. Understanding this evolution is of fundamental importance to understanding correlated systems and is obviously also central to ever being able to use Mott insulators in a controlled way in applications. From this perspective, NiO can play the role of the simplest canonical Mott insulator, analogous to the role of the hydrogen atom in understanding atomic structure, in unraveling the physics of doped Mott insulators. However, this still hinges on the availability of computational methods that can accurately incorporate electronic correlations in realistic solid structures. One such method is the stochastic quantum Monte Carlo (QMC). Relatively recent advances both in computer hardware and in algorithms and software have led to emerging applications of the QMC to real, crystalline solids, typically with results that surpass DFT for systems with important electronic correlations such as TMOs or systems in which dispersive (van der Waals) interactions are important [24–38]. In this work, we use QMC to study the effect of point defects, a substitutional K dopant in antiferromagnetic type II (AFM-II) NiO, as well as the effect of a Ni or O vacancy. We calculate defect formation energies and also study how charge and spin densities are affected by the point defect. We also compare our results with those obtained within the DFT + U scheme of DFT. In particular, we compare the defect energetics as well as the charge- and spin-density distributions. Perhaps not surprisingly, we find that the DFT + U makes significant errors in the spin and charge distributions, especially in Ni atoms but also at O sites and at the K site; at the latter spin and charge densities from the DFT + U are much lower than those from the diffusion Monte Carlo (DMC). These errors are at least in part due to the problem DFT-based approaches have in correctly obtaining both $3d$ charge and spin densities as well as the exchange-correlation energies stemming from these localized orbitals, especially in $3d$ TMOs [30,39].

II. METHODOLOGY

In these QMC studies, we primarily employed the fixed-node diffusion Monte Carlo method [40,41] as implemented in the QMCPACK code [42]. In order to describe ion-electron and electron-electron correlations in the QMC trial wave functions, we used single Slater-Jastrow wave functions with one- and two-body variational Jastrow coefficients. Cutoffs for the one- and two-body terms were set at the Wigner-Seitz radius of the supercell, and B-spline coefficients were used. DFT single-particle Kohn-Sham orbitals for the initial QMC Slater determinant trial wave function were generated using a plane-wave basis set with the QUANTUM ESPRESSO 5.3.0 code [43] with a 400-Ry kinetic energy cutoff and a $4 \times 4 \times 4$ k-point grid. We used either the Perdew-Zunger [44] local spin density approximation or the Perdew-Burke-Ernzerhof (PBE) parametrization [45] of the generalized gradient approximation (GGA) exchange-correlation functionals. For the localized d orbitals, we used the DFT + U method [46] within which on-site Coulomb interactions are taken into account by a Hubbard correction [47]. We also compared the GGA + U calculations with calculations using the DFT + U formulation of Lichtenstein, Anisimov, and Zaane [48] with the PBE GGA and one U and one J parameter with $U = 5.7$ eV and $J = 1.0$ eV for NiO and K-doped NiO. The only discernible difference was that $U + J$ led to a very slight increase in the localized Ni moment, from about $1.72\mu_B$ to $1.74\mu_B$. Therefore, we based all our analyses on results using the simpler DFT + U formulation of Dudarev.

Norm-conserving pseudopotentials for this study (Ni, O, and K) were generated with a plane-wave basis set using the OPIUM package [49]. The accuracy of the Ni pseudopotential was demonstrated in a previous DMC study for bulk AFM-II NiO [50]. In addition, the K pseudopotential in this study also provided excellent descriptions of the physical properties of bulk metal bcc K within the DMC (see the Supplemental Material [51]). In order to reduce the one-body finite-size effects from the periodic supercell DMC calculations, we used twist-averaged boundary conditions [52]. In addition, we applied the modified periodic Coulomb interaction [53] and Chiesa-Ceperley-Martin-Holzmann kinetic energy correction [54] to reduce the two-body finite-size effects. Because the DMC provides a "mixed" estimate of the density (a mixture between the fixed node density and the variational Monte Carlo (VMC) one), we have corrected the mixed estimates by extrapolation to obtain "pure" estimates of the density, reflecting the fixed-node wave function alone. This is a general property of the DMC method for operators that do not commute with the Hamiltonian. In order to obtain pure estimates of spin and charge density, we used the extrapolation formula [40]

$$\rho_{\mathrm{est},X} = 2\rho_{\mathrm{DMC,mixed},X} - \rho_{\mathrm{VMC},X}, \tag{1}$$

where X denotes spin or charge, and $\rho_{\mathrm{VMC},X}$ is the spin or charge density from the optimized VMC wave function.

Calculations to optimize the Hubbard U parameter and for the equation of state for pure rock-salt NiO used a 16-atom supercell. For all other calculations, structural relaxations started by generating 64-atom supercells for NiO and NiO with a single substitutional K dopant. These supercells were relaxed (lattice parameters and internal coordinates) on a $2 \times 2 \times 2$ k-point grid using FHI aims [55] until the maximum Hellman-Feynman force on any one atom was below 0.005 Å/eV. The lattice constants for the 64-atom NiO and K-doped NiO supercells were 8.397 and 8.445 Å, respectively. These cells as well as NiO with oxygen and nickel vacancies were subsequently subjected to relaxing the internal coordinates while keeping the lattice parameters fixed at the bulk values using the GGA + U in the projector augmented wave method [56,57] as implemented with the Vienna *Ab initio* simulation package VASP [58,59] with a kinetic energy cutoff of 400 eV and a $2 \times 2 \times 2$ k-point grid. Structures were relaxed until the maximum Hellman-Feynman force on any atom was below 0.01 eV/Å. For further information, see Supplemental Material [51].

VASP [58,59] was only used for structural relaxation. All other reported values for the GGA + U were obtained using QUANTUM ESPRESSO [43] with the same norm-conserving pseudopotentials as the QMC calculations.

III. RESULTS AND DISCUSSION

The optimal value of the Hubbard U is usually chosen empirically by matching some specific electronic property such as the band gap to experimental values, or it is arrived at self-consistently [60]. The value of U will then typically depend on the specific exchange-correlation functional used, with different exchange-correlation functionals arriving at different values of U even for the same structural environment. While there exist DFT + U schemes with multiple parameters, e.g., U parameters on $3d$ and oxygen $2p$ orbitals, to fit different values such as band-gap and defect energies, the cost of expanding the parameter set to optimize the DMC nodal surface can quickly become intractable and make the computational cost prohibitive. Moreover, the excellent comparison with experimental values that we obtain with a single U parameter indicates that expanding the parameter space may not be worth the very large increase in computational cost.

In this work, for our DMC calculations we use U as a variational parameter in the QMC trial wave function: the best nodal surface is obtained by the optimal value of U which minimizes the total energy within DMC, e.g., as performed in Refs. [29–31]. The amount of exact exchange in a hybrid functional can also be used in a similar way (see, for example, Refs. [61,62]).

In order to arrive at an optimal U for the wave-function nodal surface for AFM-II NiO, we computed the DMC total energy of NiO as a function of U. In the optimization, we used a supercell consisting of eight formula units (f.u.) of NiO (16 atoms and 192 valence electrons total) in the DMC calculations (Fig. 1).

Figure 1(a) shows the calculated DMC total energy as a function of the Hubbard U for the LDA + U and GGA + U trial wave functions. Without a Hubbard U ($U = 0$), one can see that there is a significant energy difference of 0.37(2) eV/f.u. between DMC total energies evaluated using

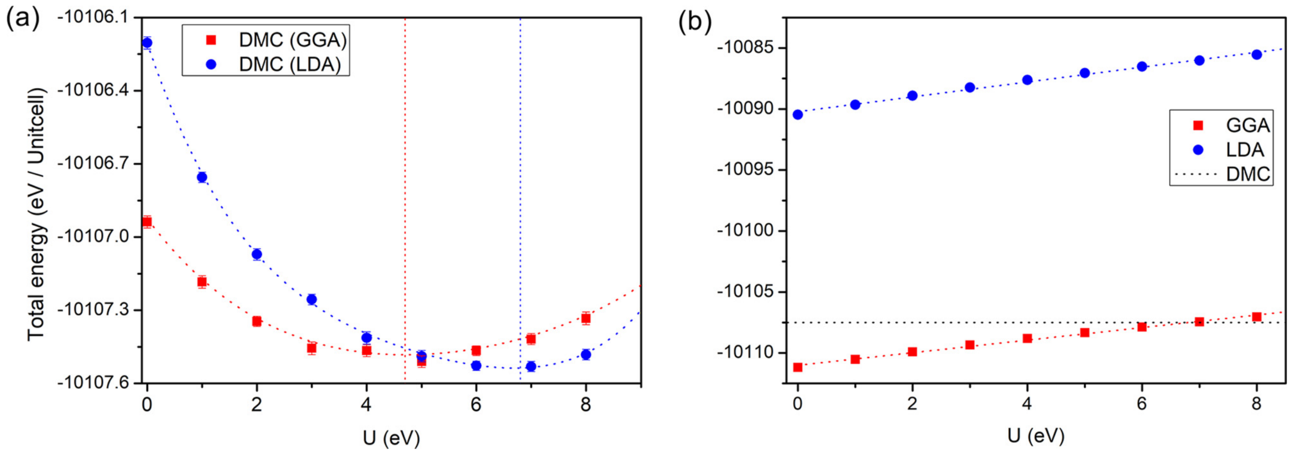

FIG. 1. (a) DMC total energy of NiO as a function of U in the LDA and GGA trial wave function. (b) LDA and GGA total energy as a function of the value of U. The dotted horizontal line indicates the DMC total energy with the optimal value of U.

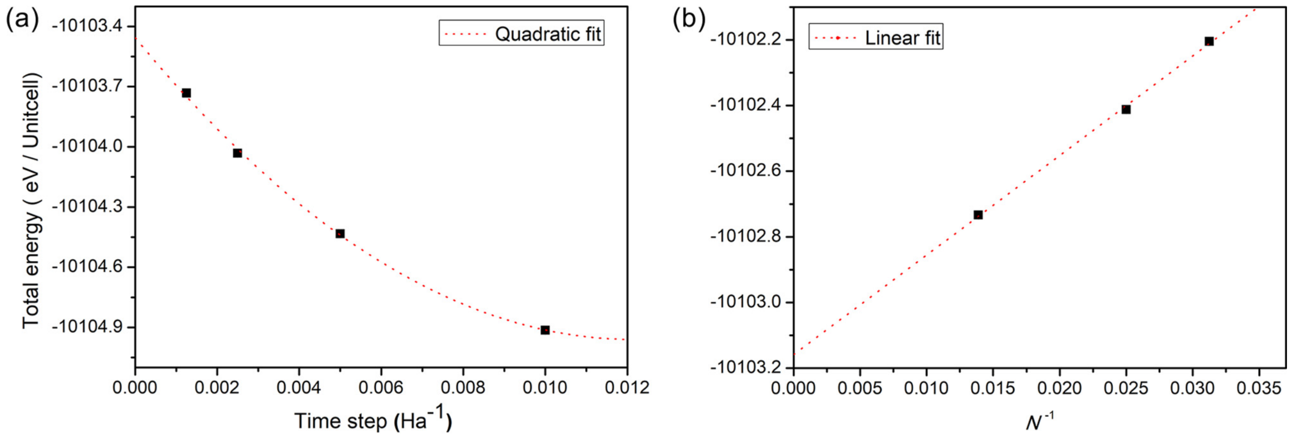

FIG. 2. (a) DMC total energy of AFM-II NiO as a function of the time step. The dotted line indicates a quadratic fit. (b) DMC total energy of NiO as a function of $1/N$, where N is the total number of atoms in the supercell. The dotted line indicates a simple linear regression fit.

LDA and GGA initial trial wave functions. As U increases, the DMC total energies decrease rapidly as the wave-function nodal surface is modified by the on-site Coulomb repulsion. Optimal values of U (U_{opt}) were obtained through a quadratic fit to the LDA- and GGA-based energies and were estimated to be 6.8(4) and 4.7(2) eV, respectively. Even though the optimal values for U are different for the LDA and GGA functionals, the minimum DMC energies obtained with the LDA and GGA wave functions at their respective U_{opt} values are very close, $-10\,107.54(1)$ eV/unit cell (LDA) and $-10\,107.50(1)$ eV/unit cell (GGA). In contrast, and as expected due to the lack of a variational principle with respect to U, the DFT + U total energy increases with U for both the LDA + U and the GGA + U [Fig. 1(b)].

In order to assess the accuracy of the description of NiO obtained with the DFT(GGA) + U at U_{opt} and the DMC with the GGA + U_{opt} nodal surface, we calculated the equation of state for AFM-II NiO using the GGA + U and DMC. In the DMC calculations, time-step convergence and finite-size analysis were fully taken into account (Fig. 2). The DMC total energy at zero time step was obtained by extrapolating the DMC energy at DMC time steps of 0.01, 0.005, 0.0025, and 0.00125 Ha^{-1} using a quadratic function [Fig. 2(a)]. Beyond full consideration of one-body finite-size effects by applying twist-averaged boundary conditions with a total of 64 twists, we additionally extrapolated the DMC results at zero time step to infinite size using 8, 10, and 18 f.u. supercells in order to remove two-body finite-size effects [Fig. 2(b)].

From the calculated NiO total energies as a function of the volume of the unit cell, we obtained the equilibrium lattice parameter, bulk modulus, and cohesive energy using the Vinet function. The results for the lattice parameter and bulk modulus using the GGA + U and DMC are quite comparable (Fig. 3 and Table I). However, the GGA + U significantly underestimates the cohesive energy compared to the DMC and experimental values [63]. In contrast, the DMC-computed physical properties of AFM-II NiO are in excellent agreement with experimental results. Moreover, our DMC results evaluated using the DFT + U_{opt} trial wave function and nodal surface exhibit a good agreement for the lattice constant and cohesive energy with previous DMC results [50] which used a DFT trial wave function without any Hubbard U [64]. This leads us to conclude that trial wave functions for NiO based on the LDA or LDA + U orbitals experience a similar degree of fixed node error cancellation, despite the fact that a Hubbard U correction does result in a better nodal surface on the basis of the variational principle.

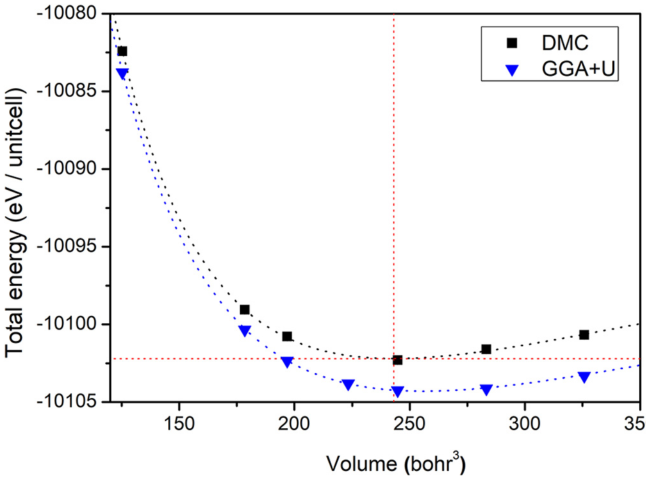

FIG. 3. GGA + U and DMC total energy of AFM-II NiO as a function of the unit cell volume. The dotted red line indicates the DMC total energy at the equilibrium unit cell volume as estimated by the Vinet fit.

TABLE I. Values of the lattice constant (a), bulk modulus (B_0), and cohesive energy (E_{coh}) for AFM-II NiO obtained from a Vinet fit of the equation of state (Fig. 3) computed using the GGA + U and DMC at $U = U_{\mathrm{opt}}$ and a 16-atom AFM-II NiO supercell.

Method	a (Å)	B_0 (GPa)	E_{coh} (eV/f.u.)
GGA + U	4.234	192	8.54
DMC[a]	4.157(3)	196(4)	9.44(2)
DMC (current)	4.161(7)	218(14)	9.54(5)
Experiment[b]	4.17	145-206	9.5

[a] From Ref. [50].

[b] From Ref. [63].

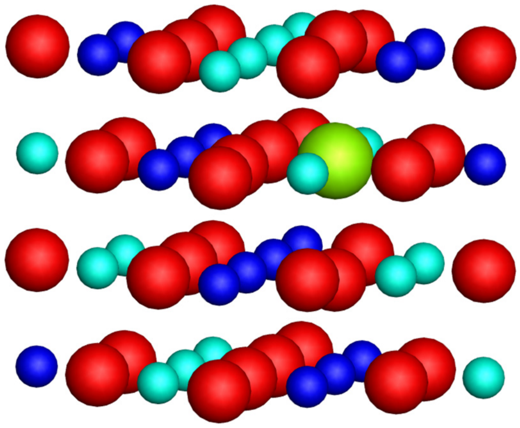

FIG. 4. Structure of 64-atom K-doped NiO. Red spheres represent oxygen; blue and teal spheres, the two nickel spin species; and green sphere, potassium. The sizes of the spheres represent their ionic radii. Buckling of the oxygen atoms' positions near the potassium site is clearly visible.

TABLE II. Calculated formation energy of a K dopant (E_f) NiO under O-rich conditions and optical gap (E_g) for NiO and K-doped NiO in a 64-atom supercell. Energies are given in units of eV.

Method	E_f (K)	E_g (NiO)	E_g (KNiO)
GGA	1.9	1.4	0.7
GGA + U	0.6	3.6	2.9
DMC[a]	—	4.7(2)	—
DMC (current)	1.3(3)	5.8(3) 5.0(7)[b]	4.8(4)
Expt.	—	4.3[c]	3.7–3.9[d]

[a]From Ref. [50].

[b]Optical gap calculated in a 128-atom supercell.

[c]From Refs. [2] and [70–72].

[d]From Ref. [22].

We now turn to K-doped AFM-II. GGA + U and DMC calculations were performed on the relaxed structure (relaxed using the GGA + U as explained earlier) using the same value of U_{opt} (4.7 eV) as for NiO. We considered $K_{0.03}Ni_{0.97}O$ including a total of 64 atoms (759 electrons) with K substituting for one Ni. The concentration of K was significantly lower than the reported maximum concentration of $K_{0.25}Ni_{0.75}O$ [22]. A total of eight twists under twist-averaged boundary conditions were used for K-doped NiO in order to eliminate one-body finite-size effects. As can be seen in Fig. 4, the light oxygen atoms are displaced away from the K atom with the near-neighbor K-O bond increasing by 10.24%, to 2.33 from 2.10 Å. In contrast, the displacement of the Ni atoms nearest the K site is negligible, only about 0.42%, from 2.96 to 2.99 Å.

With the relaxed NiO and K-doped NiO structures we first computed optical gaps for NiO and K-doped NiO to assess the effect of the K dopant on the energy gap. Since the smallest energy gap within the PBE + U calculation was observed at the Γ symmetry point in the Brillouin zone of a 64-atom supercell, we also calculated the DMC direct gap at the corresponding symmetry point. The DMC optical gap can be estimated by computing $E_{\text{ph}} - E_g$, where E_{ph} and E_g represent the total energies of the state with a particle-hole excitation and of the ground state, respectively. The DMC value for E_{ph} was computed by promoting an electron from the valence state at the Γ symmetry point to the lowest conduction state in the initial trial wave function and subsequently preserving the nodal surface of the wave function under the fixed-node approximation. While we cannot prove that this excited-state wave function will maintain its orthogonality to the ground state, this procedure is commonly used and, in practice, usually gives good results [65,66].

It is not surprising that the GGA band gaps for NiO and K-doped NiO are found to be significantly smaller than the values obtained from the DMC or experiments, as can be seen in Table II. When a Hubbard U of 4.7 eV is introduced, the band gaps for both NiO and K-doped NiO increase significantly, but the values are still smaller than the experimental value of 4.3 eV. On the other hand, the DMC significantly overestimates the optical gap for NiO compared to experimental values. Because of the possibility of large finite-size effects on the band gap, we also computed the NiO band gap using a larger supercell consisting of 128 atoms, for which the band gap was 5.0(7) eV. This value is likely smaller than the band gap using the smaller supercell, but the large statistical error for the 128-atom supercell does not permit us to conclusively claim that the band gap decreases with increasing supercell size. It is also likely still significantly larger than the experimental gap. Our DMC NiO band gap is larger than a previously reported [50] DMC direct band gap evaluated without a Hubbard U in the trial wave function [67]. This led us initially to speculate that the discrepancy between our DMC band gap and experiments may be due to a large fixed-node error in the excited state at Hubbard $U = U_{\text{opt}}$, where U_{opt} is the value that minimizes the DMC ground-state energy. However, calculations of this energy gap as a function of U showed that the energy gap is fairly constant for $U \gtrsim 2.0$ eV (for details, see the Supplemental Material [51]). Rather, we speculate that the large gap is mostly due to finite-size effects, which is partly supported by the results from the 128-atom supercell. On the other hand, upon doping with K, we find that the band gap in NiO is significantly decreased by a substitutional K dopant in the 64-atom supercell, or 3% doping, in both the DMC and the GGA + U, by 1.1(5) and 0.7 eV, respectively. This is consistent with the DFT density of states, which indicates that the K substitution leads to a state just above the lower Ni d bands (Fig. 5). The GGA + U results indicate that K is an acceptor dopant, with an unoccupied state (hole) just above the Fermi surface. For comparison, experiments [22] found a decrease of 0.4–0.6 eV in the band gap with a 25% substitutional doping with potassium.

Next, we computed the formation energy $E_f(\text{K})$ of a K dopant in NiO in order to assess the thermodynamic stability of K doping. Using the standard equation [68,69] $E_f(\text{K}) = E_{\text{KNiO}} - E_{\text{NiO}} - (\mu_{\text{K}} - \mu_{\text{Ni}})$, where E_{KNiO}, E_{NiO}, μ_{K}, and μ_{Ni} represent the total energy of doped NiO, pure NiO, and the chemical potential K of dopant and Ni, respectively. In general, the reference chemical potential is obtained from the total energy of the bulk system for the corresponding element, but the choice of reference for the Ni chemical potential depends strongly on the growth conditions (O rich or Ni rich) used to make a NiO film. Under O-rich conditions, the oxygen

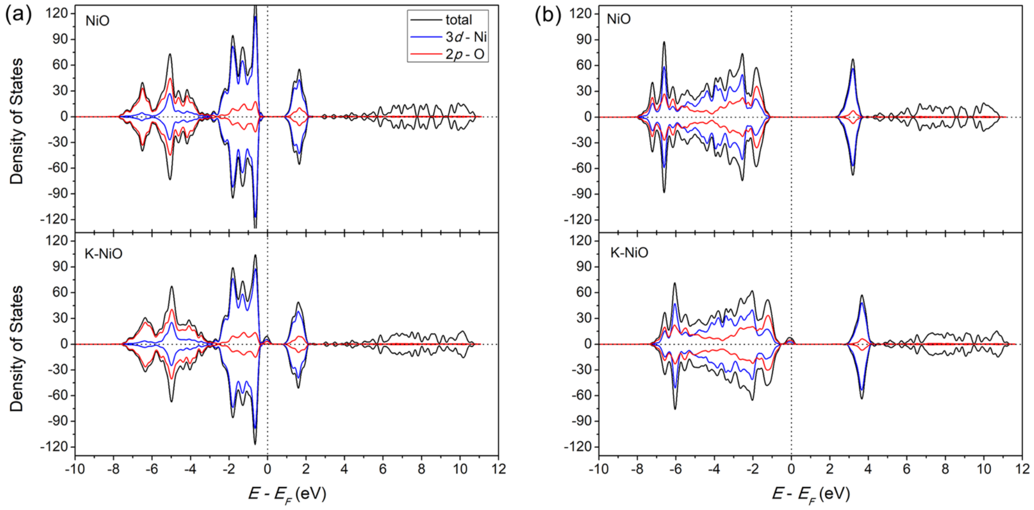

FIG. 5. Spin-resolved density of states and projected density of states in the Ni $3d$ and O $2p$ states for NiO and K-NiO using (a) the GGA and (b) the GGA + U. The K dopant introduces states near the Fermi energy.

chemical potential μ_{O} can be evaluated [50] by computing $\mu_{\mathrm{O}} \approx \frac{1}{2}E_{\mathrm{O}_2}$, where E_{O_2} is the total energy of an oxygen dimer. We can then calculate the Ni chemical potential (μ_{Ni}) using the equilibrium condition of NiO, $\mu_{\mathrm{NiO}} = \mu_{\mathrm{Ni}} + \mu_{\mathrm{O}}$. Note that we used the total energy of NiO as the reference energy for μ_{NiO}. In contrast, the total energy of bulk Ni is required to obtain a reference energy for μ_{Ni} under Ni-rich conditions. In this study, we focused on the formation energy under O-rich conditions due to potential uncertainties in describing the bulk ferromagnetic Ni metal in the DMC with a single Slater determinant. We calculated the reference energy for the K chemical potential including contributions from the ionic bonding between K^{+} and O^{-2} ions using the equilibrium condition $\mu_{\mathrm{K_2O}} = 2\mu_{\mathrm{K}} + \mu_{\mathrm{O}}$, where $\mu_{\mathrm{K_2O}}$ denotes the chemical potential of bulk antifluorite $\mathrm{K_2O}$, which can be obtained from the total energy of the corresponding structure.

Table II lists the calculated formation energy of a substitutional K dopant near the center of a 64-atom supercell. Both the GGA + U and the DMC formation energies for a potassium substitutional dopant are significantly lower than the formation energies for oxygen or nickel vacancies under oxygen-rich conditions (see below), indicating the relative stability of K doping under these conditions. Also, the GGA + U K-dopant formation energy is found to be significantly lower than the DMC formation energy. This is consistent with the GGA + U underestimating the cohesive energy for NiO compared to DMC (and experiments). However, the difference in K-dopant formation energy between the GGA + U and the DMC is about 46%, compared to the much smaller 10% difference in the cohesive energy of NiO.

In order to visualize the electron spin density distributions in the presence of a substitutional dopant and to analyze any discrepancy between the GGA + U and the DMC spin densities, we calculated the total electron charge density $\rho_{\mathrm{charge}} = \rho_{\mathrm{up}} + \rho_{\mathrm{down}}$ and spin density $\rho_{\mathrm{spin}} = \rho_{\mathrm{up}} - \rho_{\mathrm{down}}$, where ρ_{up} and ρ_{down} represent the charge density for up- and down-spin electrons, respectively. Figure 6 shows spin densities for K-doped NiO obtained using the GGA + U and DMC, and Fig. 7 shows the difference in spin density between the DMC and the GGA + U. In order to reduce the noise in the DMC spin densities, we averaged them over symmetries and also filtered some high-frequency spatial noise (see the Supplemental Material for details [51]). The figures show a weak induced $2p$ spin density at the oxygen sites, with a total moment of 0. While the DMC data are noisier because of the statistical sampling, the induced spin densities are higher at the oxygen sites for the DMC than for the GGA + U. Furthermore, in the GGA + U, the spin density at the K site is completely negligible; in the DMC it is clearly nonzero but small. The lower panels in Fig. 6 clearly show the arrangement of the Ni $3d_{x^2-y^2}$ orbitals and the oxygen $2p$ orbitals leading to antiferromagnetic superexchange between the Ni sites. Note that the oxygen $2p$ orbitals in the GGA + U are aligned along the (110) direction (diagonally in the figure) and not along the (100) direction. There is some distortion in the GGA + U spin density at the oxygen sites (lower left panel in Fig. 6), especially directly under the dopant. The DMC spin densities at the oxygen sites show more distortion, especially on the (110) line (lower right panel in Fig. 6). In the plane of the K dopant, the oxygen $2p$ orbitals are clearly distorted (top panels in Fig. 6) and aligned directly along the (100) and (010) directions connecting the nearest antiferromagnetically arranged Ni sites around the K site. The bottom panels also indicate that there is a slight difference in the spin density at the oxygen site at the center of the planes: this site is directly underneath the K site, and this oxygen spin density is not symmetric across the $(\bar{1}10)$ line with more negative (blue) than positive spin density. The distortion of the oxygen $2p$ orbitals near the K site is captured qualitatively by both the GGA + U and the DMC calculations but is quantitatively different because of the higher induced spin density in the oxygen $2p$ orbitals in the DMC. Figure 8 shows a one-dimensional plot of the charge density obtained along the (111) direction by applying all 48 rotational symmetry operations corresponding to cubic symmetry to the charge density centered around the central Ni (left panel) or the impurity atom (right panel). The figure shows that the charge density at the central K atom is rather delocalized and, also, shows a small change (decrease)

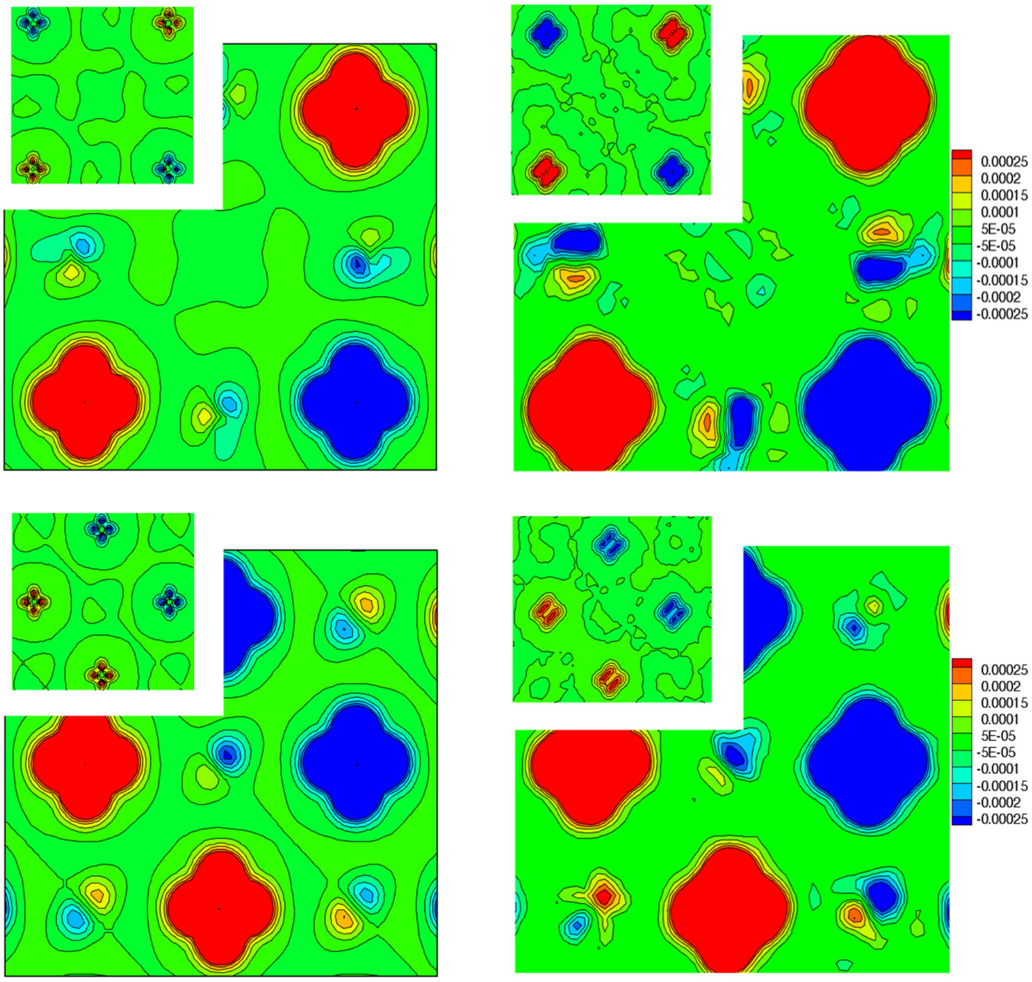

FIG. 6. Two-dimensional contour plots of GGA + U (top left) and DMC (top right) spin densities in the (001) basal plane containing the K dopant in K-doped NiO, in units of Å^{-3}. The K dopant is located at the center in the contour plots. Lower panels show the corresponding spin densities in a lower (001) basal plane without a K dopant. Insets: The same densities on a scale from -0.0075 to 0.0075 Å^{-3}.

in the charge density at the near-neighbor oxygen sites (small bumps near 3.66 and 10.97 Å) as well as an increased charge at the Ni sites (near 0.00 and 14.63 Å). The hole density arising from the monovalent dopant primarily resides at the K site, with additional charge distortions at O and Ni sites in the supercell.

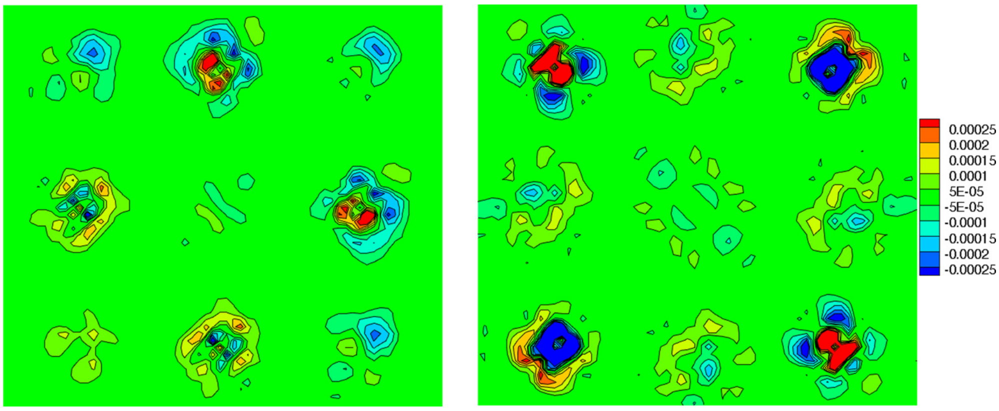

FIG. 7. Two-dimensional contour plots of the difference between the DMC and the GGA + U spin densities. The left panel shows the spin density difference in a (001) basal plane below the central plane with the K dopant; the right panel shows the spin density difference in the central (001) plane, with the K dopant at the center of the figure. The color scale goes from -0.00025 to $+0.00025$ Å^{-3}. The DMC Ni spin densities are slightly more extended than the GGA + U ones.

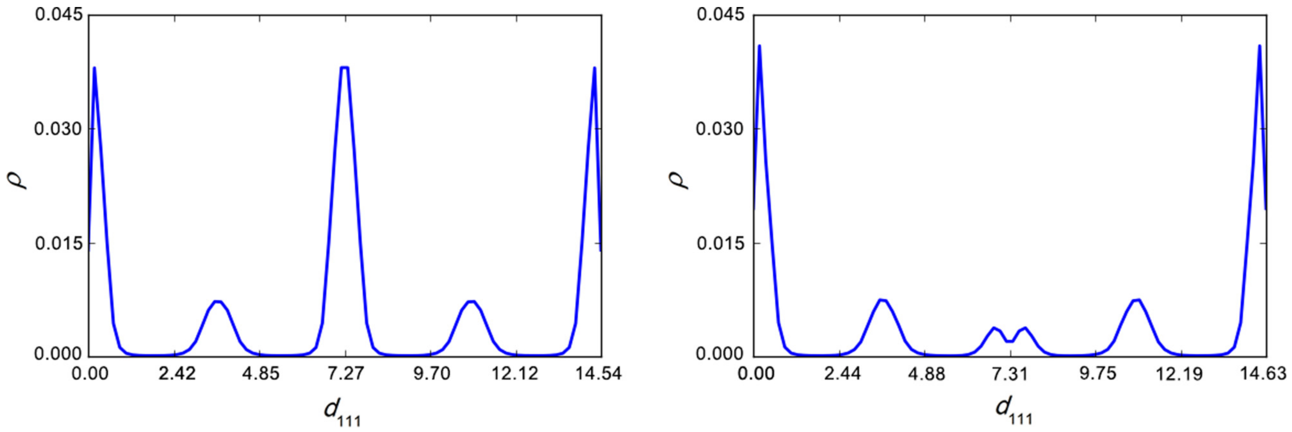

FIG. 8. One-dimensional symmetrized plots of the charge density, in units of Å^{-3}, along the (111) direction (d_{111}, in units of Å) in NiO (left panel) and K-doped NiO (right panel) with a central Ni (left panel) or K (right panel) atom. The figures show an increase in the Ni charge in the presence of K (right panel, near 0 and 14) as well as a small polarization at the O sites (right panel, near 3 and 10).

Figure 7 shows contour plots of the spin density difference between the DMC and the GGA + U calculations. The left panel shows the spin density difference in a (001) basal plane not containing the K dopant, and the right panel shows the spin density difference in the central (001) plane containing the K dopant, with the K site at the center of the figure. The figure clearly shows a difference in the spin density at the Ni sites: the DMC spin density is less than the DFT + U one near the Ni cores, but the DMC spin density is more extended (this shows up as, e.g., the blue layer around the red core as at the top Ni site in the left panel in Fig. 7). The right panel in Fig. 7 shows that this difference between the DMC and the GGA + U Ni spin densities is increased in the plane of the dopant.

In order to quantify the spin and charge density differences between the DMC and the GGA + U results, we computed the root-mean-square deviation (RMSD) of the charge and spin densities as [73]

$$\mathrm{RMSD}(\rho) = \sqrt{\frac{\sum_{i=1}^{N}(\rho_{\mathrm{DFT}}(R_i) - \rho_{\mathrm{DMC}}(R_i))^2}{N}}, \tag{2}$$

where $\rho_{\mathrm{DFT}}(R_i)$, $\rho_{\mathrm{DMC}}(R_i)$, and N denote the DFT and DMC charge or spin density at grid point R_i and the total number of grid points, respectively. The results are listed in Table III. The calculated RMSD(ρ_{charge}) and RMSD(ρ_{spin}) for NiO and K-doped NiO are almost identical: there are differences between the DMC and the GGA + U charge and spin density distributions but the presence of the K dopant does not significantly change the average of the charge and spin density distributions in the supercell, as indicated by the first two rows in the table. In order to quantify the charge and spin density differences between the DMC and the GGA + U at the Ni and O sites (Fig. 7), we computed the charge and spin density RMSD in spherical volumes with a radius equal to half the Ni-O bond length (1.16 Å) centered at the Ni sites, $\rho_{\mathrm{type}}^{\mathrm{Ni}}$, or the O sites, ρ_{type}^{O}, where *type* is *charge* for the charge density and *spin* for the spin density. We also calculated RMSD values for charge and spin density average only over the Ni or O sites that are near neighbors to the K-dopant site, denoted RMSD($\rho_{\mathrm{type}}^{X(\mathrm{NN})}$), where X is Ni or O. We first discuss the RMSD values for charge densities. There is little change in RMSD(ρ_{charge}) in the presence of the dopant: while there are differences between the DMC and the GGA + U charge densities, they are not significantly changed over the whole supercell. In contrast, RMSD($\rho_{\mathrm{charge}}^{\mathrm{Ni}}$) and RMSD($\rho_{\mathrm{charge}}^{\mathrm{O}}$) do change in the presence of the dopant, especially RMSD($\rho_{\mathrm{charge}}^{\mathrm{Ni}}$). This indicates that the charge distribution at the Ni sites changes more in the DMC in the presence of the dopant than it does in the GGA + U. On the other hand, there is a much smaller difference between RMSD($\rho_{\mathrm{charge}}^{\mathrm{Ni}}$) and RMSD($\rho_{\mathrm{charge}}^{\mathrm{Ni(NN)}}$) and between the corresponding RMSD values for O. This leads us to conclude that the difference in charge distribution between DMC and GGA + U when the dopant is introduced is not confined primarily to sites near the dopant but is more evenly distributed throughout the supercell.

Next, we discuss the RMSD values for the spin density. We focus on the Ni spins as an analysis of the O spins that is entirely analogous. The $\rho_{\mathrm{spin}}^{\mathrm{Ni}}$ RMSD is significantly larger, 0.435, than the supercell spin density RMSD, RMSD(ρ_{spin}) = 0.077, consistent with the Ni spin density difference shown in

TABLE III. Calculated RMS deviation of spin and charge electron densities for NiO and K-doped NiO. Statistical errors in the RMSDs are below 10^{-7}.

	NiO	K-doped NiO
RMSD(ρ_{spin}) (10^{-3})	0.061	0.077
RMSD(ρ_{charge}) (10^{-3})	0.148	0.155
RMSD($\rho_{\mathrm{charge}}^{\mathrm{Ni}}$) ($10^{-3}$)	1.106	1.154
RMSD($\rho_{\mathrm{charge}}^{\mathrm{O}}$) ($10^{-3}$)	0.193	0.219
RMSD($\rho_{\mathrm{charge}}^{\mathrm{Ni(NN)}}$) ($10^{-3}$)	—	1.131
RMSD($\rho_{\mathrm{charge}}^{\mathrm{O(NN)}}$) ($10^{-3}$)	—	0.197
RMSD($\rho_{\mathrm{spin}}^{\mathrm{Ni}}$) ($10^{-3}$)	0.376	0.435
RMSD($\rho_{\mathrm{spin}}^{\mathrm{O}}$) ($10^{-3}$)	0.135	0.174
RMSD($\rho_{\mathrm{spin}}^{\mathrm{Ni(NN)}}$) ($10^{-3}$)	—	0.433
RMSD($\rho_{\mathrm{spin}}^{\mathrm{O(NN)}}$) ($10^{-3}$)	—	0.163
RMSD($\rho_{\mathrm{spin}}^{\mathrm{K}}$) ($10^{-3}$)	—	0.093

Fig. 7. Moreover, RMSD($\rho_{\text{spin}}^{\text{Ni}}$) increases more in the presence of the dopant, from 0.376 to 0.435, than the corresponding supercell value RMSD(ρ_{spin}) (0.061 to 0.077). This shows that there is indeed a quantifiable, but small, difference in the Ni spin redistribution between DMC and GGA + U in the presence of the dopant. On the other hand, the difference between the near-neighbor spin RMSDs, RMSD($\rho_{\text{spin}}^{\text{Ni(NN)}}$) $=$ 0.433 and RMSD($\rho_{\text{spin}}^{\text{Ni}}$) $= 0.435$, in the presence of the dopant is small; just as for the charge density, the difference between DMC and GGA + U Ni spin densities in the presence of the dopant is distributed throughout the supercell and not confined to the Ni sites near the dopant. Finally, RMSD(ρ_{spin}^{K}) $= 0.093$ shows, as expected, a difference between the DMC and the GGA+U spin distribution at the K site.

In order to correlate differences between the DMC and GGA + U (spin) densities and the total energy differences, we recall that the GGA + U total energy for NiO is close to the DMC total energy with $U = U_{\text{opt}}$. In view of the more compact DMC Ni spin densities and the higher DMC oxygen $2p$ spin densities, this suggests that there is an error cancellation in the GGA + U between more extended Ni spin densities than in the DMC but lower oxygen $2p$ spin densities. On the other hand, the formation energy of the K dopant is much lower in the GGA + U (0.59 eV) than in the DMC (1.29 eV). This makes us speculate that the difference in the dopant formation energy originates primarily in the DMC spin density at the K site, as the GGA + U has no discernible spin density at the K site, coupled with a much smaller difference in spin densities throughout the supercell.

Finally, we discuss the formation energies of Ni (O) neutral vacancies in NiO under oxygen-rich conditions, as well as the spin and charge densities of systems with Ni vacancies. We here consider the formation of a Ni (O) vacancy in NiO under O-rich conditions. We removed a Ni (O) from the 64-atom NiO supercell and relaxed the internal coordinates of the resulting structure. The formation energy E_f of a neutral single vacancy in NiO can be calculated as $E_f = E_{\text{NiO:vac}} - E_{\text{NiO}} + \mu_{\text{vac}}$, where E_{NiO}, $E_{\text{NiO:vac}}$, and μ_{vac} are the total energy for NiO with a defect, total energy for stochiometric NiO, and chemical potential of the vacancy species (Ni or O).

DMC and DFT + U formation energies for neutral O [E_f(O)] and Ni [E_f(Ni)] vacancies in NiO as well as RMSD values for charge and spin density distributions are summarized in Table IV. The GGA + U value, 6.2 eV, for E_f(O) with the Hubbard U at $U = U_{\text{opt}}$ is smaller than the previously reported DMC value, 7.2 eV, using a $U = 0$ trial wave function and nodal surface [50]. However, we note that our computed values for E_f(O) using the GGA + U and DMC are comparable, at 6.2 and 6.6 eV, respectively. This leads us to conclude that the GGA + U with U = U$_{\text{opt}}$ does a reasonably good job of describing not only the ground-state energy of NiO but also the energetics of single neutral oxygen vacancies. In contrast, the DMC formation energy E_f(Ni) for the neutral Ni vacancy is significantly higher (and positive), at 3.5 eV, than the GGA + U energy, which is negative (−0.9 eV). The latter would imply that neutral Ni vacancies would form spontaneously under oxygen-rich conditions. This disagrees with the calculations of defect energies by Zhang *et al.* [74] using the GGA + U with both U and J parameters. However, Zhang *et al.* used $U = 6.3$ eV and $J = 1$ eV and a less stringent condition on geometry optimization (Hellman-Feynman forces relaxed to within 0.05 eV/Å). We know from our own calculations that not relaxing the geometry with a Ni vacancy increases its formation energy rather substantially, from −0.9 to +0.1 eV. Furthermore, the NiO band gap obtained by Zhang *et al.* was 3.1 eV, considerably lower than the experimental value of 4.3 eV and our own GGA + U value of 3.59 eV. We believe that the more stringent conditions on our GGA + U calculations lead to a more accurate value for E_f(Ni) within the GGA + U. Therefore, we conclude that the GGA + U erroneously gives a negative formation energy for a neutral Ni vacancy point defect under oxygen-rich conditions.

TABLE IV. Calculated formation energies, in eV, of a single neutral O and Ni vacancy in NiO under oxygen-rich conditions and spin density RMSD at the Ni sites.

Method	E_f(O)	E_f(Ni)
GGA + U	6.2	−0.9
DMC[a]	7.2(2)	—
DMC	6.6(4)	3.5(4)
RMSD(ρ_{charge}) (10^{-3})	0.151	0.146
RMSD($\rho_{\text{charge}}^{\text{Ni}}$) ($10^{-3}$)	1.108	1.090
RMSD($\rho_{\text{charge}}^{\text{O}}$) ($10^{-3}$)	0.202	0.187
RMSD($\rho_{\text{charge}}^{\text{Ni(NN)}}$) ($10^{-3}$)	1.056	1.064
RMSD($\rho_{\text{charge}}^{\text{O(NN)}}$) ($10^{-3}$)	0.191	0.176
RMSD(ρ_{spin}) (10^{-3})	0.069	0.065
RMSD($\rho_{\text{spin}}^{\text{Ni}}$) ($10^{-3}$)	0.397	0.408
RMSD($\rho_{\text{spin}}^{\text{O}}$) ($10^{-3}$)	0.160	0.132
RMSD($\rho_{\text{spin}}^{\text{Ni(NN)}}$)) ($10^{-3}$)	0.395	0.440
RMSD($\rho_{\text{spin}}^{\text{O(NN)}}$) ($10^{-3}$)	0.163	0.119

[a] From Ref. [50].

The top row in Fig. 9 depicts the DMC spin density in a basal (001) plane without (left panel) and with (right panel) the Ni vacancy. The bottom row depicts the corresponding spin density difference between the DMC and the GGA + U. The top left panel now clearly shows an asymmetric spin density at the central O site with a net negative spin density. Similarly, the top right panel indicates a negative spin density at the oxygen sites: this suggests that the hole density is primarily located at the oxygen-site near neighbors to the Ni vacancy. In addition, the bottom row in Fig. 9 shows that the DMC Ni spin density is higher than the GGA + U and that the DMC oxygen spin density in the plane of the vacancy is more localized towards the vacancy than the GGA + U. Figure 10 shows a three-dimensional depiction of isosurfaces of the difference in charge density between the system with and that without a Ni vacancy. The “dumbbells” are all pointing towards the vacancy site, with the oxygen dumbbells’ *n*egative charge (charge repelled from the vacancy) pointing towards the vacancy, and the Ni dumbbell’s *p*ositive charge pointing towards the vacancy. This is just a manifestation of the fact that Ni near the vacancy relaxes inward toward the vacancy, whereas oxygen near the vacancy relaxes outward away from the vacancy. The symmetry of the dumbbells suggests that

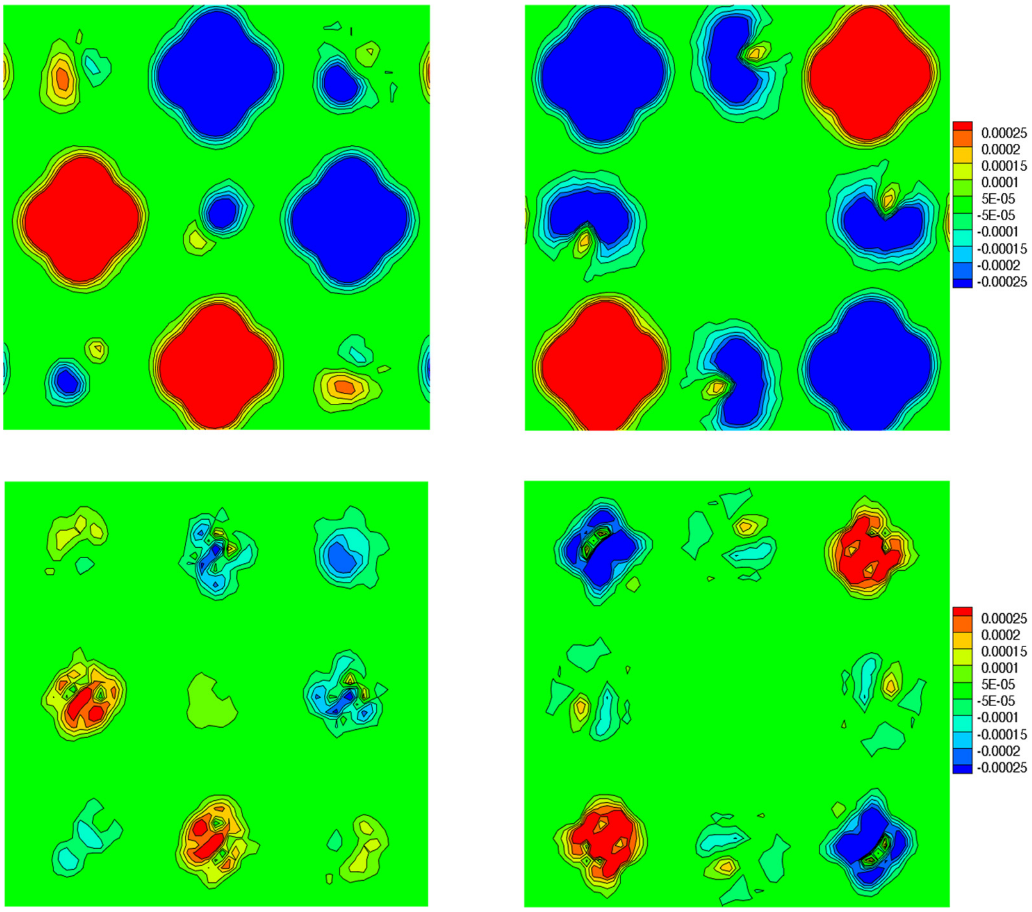

FIG. 9. Two-dimensional contour plots of the DMC spin density, in units of Å^{-3}, in the (001) basal plane without a NiO vacancy (upper left) and in the (001) basal plane containing a single neutral Ni vacancy (upper right). The Ni vacancy is located at the center of the panel. Lower panels show the difference between the DMC and the GGA + U spin densities in the same planes.

there is little net charge changed at the oxygen and Ni sites, in contrast with the spin density in Fig. 9. Figure 11 shows one-dimensional symmetrized graphs of the charge density along the (111) direction in the NiO supercell (left panel), for comparison, and in the supercell with a central Ni vacancy (right panel). Also in contrast with the K-doped supercell, the symmetrized Ni vacancy charge density shows no clear charge accumulation or depression at the oxygen sites but does show a depression of charge at the Ni sites. The hole density from the Ni vacancy resides primarily at the vacancy site, with some charge distortions at the Ni sites throughout the supercell.

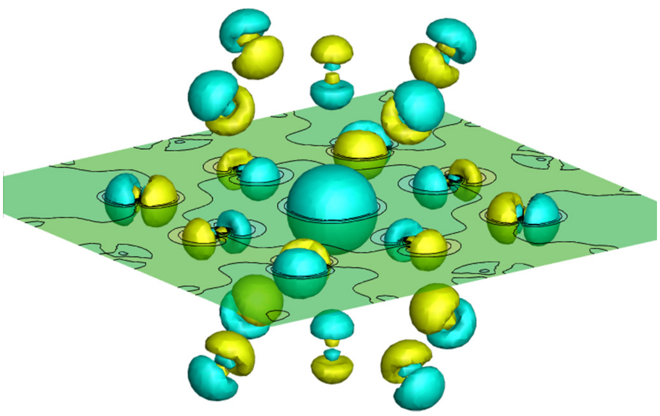

FIG. 10. Three-dimensional isosurface plot of the difference between the GGA + U charge density with and that without the Ni vacancy. Isosurfaces are at ±0.002 Å^{-3}, with gold indicating positive and teal negative.

We concluded earlier that the incorrect spin and charge distributions in the GGA + U led to underestimating the formation energy of a K dopant within the GGA + U. Similarly, we conclude that the large discrepancy in the formation energy of a Ni vacancy within GGA + U compared to DMC can be understood to arise from the qualitatively and quantitatively different charge and spin density distributions at the Ni sites where large values of the RMSD parameters were observed. As reported in Table IV, the RMSD($\rho_{\text{spin}}^{\text{Ni}}$) and RMSD($\rho_{\text{spin}}^{\text{Ni(NN)}}$) are both large, at about 0.4. Both increase in the presence of the Ni vacancy, but RMSD($\rho_{\text{spin}}^{\text{Ni(NN)}}$) increases more, from 0.395 to 0.440: the Ni vacancy has a larger impact on the spin redistribution than does the substitutional K dopant, and this redistribution is poorly captured by the DFT + U. Similarly, the spin distributions at the oxygen sites are relatively poorly captured by the DFT + U, with RMSD($\rho_{\text{spin}}^{\text{O}}$) and RMSD($\rho_{\text{spin}}^{O(\text{NN})}$) being similar, at 0.160 and 0.163, respectively, for NiO. These values *decrease*, however, to 0.132 and 0.119 in the presence of the Ni vacancy, indicating a smaller difference between the GGA + U and the DMC

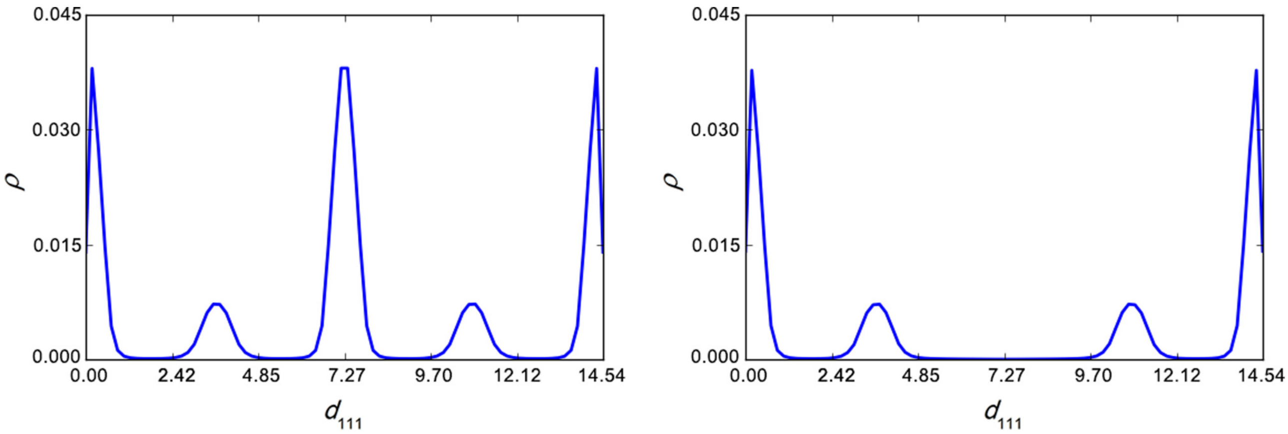

FIG. 11. One-dimensional symmetrized plots of the charge density, in units of Å^{-3}, along the (111) direction (d_{111}, in units of Å) in NiO (left panel) and NiO with a Ni vacancy at the center (right panel) with a central Ni (left panel) or Ni-vacancy (right panel) atom. The figures show a lack of hole charge accumulation as seen in K-doped NiO, with a very slight decrease in the Ni charge in the presence of a Ni vacancy (right panel, near 0 and 14).

oxygen spin density distributions in the presence of the vacancy.

IV. CONCLUSIONS

In summary, we have used highly accurate DMC as well as DFT + U (GGA + U) methods to study AFM type II NiO and its point defects, potassium substitutional dopant, and Ni and O vacancies. A potassium dopant (single hole) and Ni vacancy (two holes) point defects both lead to spin-and charge redistributions extending well beyond near neighbors to the point defect. However, for the potassium dopant the charge redistribution is at both oxygen and Ni sites, while for the Ni vacancy, it is primarily at Ni sites. Our calculations, using both the PBE + U and the QMC, show that a low dopant concentration significantly lowers the energy gap, consistent with previous experiments [22]. However, the energy gap for NiO obtained using the diffusion Monte Carlo is significantly larger than experimental values as well as previous results using the diffusion Monte Carlo [50]. Calculations of the gap as a function of U as well as for a 128-atom supercell suggest that finite-size effects contribute to this discrepancy. The defect formation energies for a K dopant and Ni vacancy differ considerably between the GGA + U and the DMC. By comparing RMS differences for charge and spin densities between the DMC and the GGA + U, both for the whole supercell and for local Ni and O sites, we conclude that the difference in defect formation energy arises primarily from the the difference in spin densities in the Ni $3d$ orbitals obtained from the GGA + U and DMC, with a smaller contribution from differences in O $2p$ spin distributions; in these cases, because of the distorted spin distributions compared to the defect-free systems, error cancellation is much smaller in the GGA + U, which increases energy differences compared to the DMC. From our results, we also conclude that previously obtained point defect formation energies based on DFT schemes are underestimated [50,74,75]. Previous predictions of the energetic stability of point defects in NiO using the typical DFT + U functional were too optimistic compared to DMC results. Correcting DFT schemes to better account for defect formation energies will obviously require a delicate balance between obtaining better spin densities and the concomitant energy changes. At the same time, it is likely that such corrections to improve defect formation energies may lead to worse estimates of other electronic properties, such as the band gap. It would be interesting in future work to compare the electronic properties obtained in DFT schemes using DMC charge densities, similar to the so-called HF-DFT scheme, in which Hartree-Fock densities are used to evaluate DFT energies [76]. The HF-DFT scheme has been shown to yield significantly better energies for so-called spin-crossover complexes [77]. These complexes have a small energy difference between high- and low-spin states that DFT fails to obtain, often even getting the wrong sign for it. In contrast, HF-DFT energies are very close to benchmark DMC energies [78]. As in our work here on NiO, the difficulty of DFT in dealing with spin-crossover complexes has been traced to the relatively poor DFT description of the Fe $3d$ orbital in these complexes. A systematic study of DMC-DFT energies may lead to a fruitful avenue for improving DFT, at least for third-row transition metal complexes, by correcting its densities, especially those on localized $3d$ orbitals.

ACKNOWLEDGMENTS

We thank Luke Shulenburger (Sandia National Laboratory) for fruitful discussions. This work was supported by the US Department of Energy, Office of Science, Basic Energy Sciences, Materials Sciences and Engineering Division, as part of the Computational Materials Sciences Program and Center for Predictive Simulation of Functional Materials. An award of computer time was provided by the Innovative and Novel Computational Impact on Theory and Experiment (INCITE) program. This research used resources of the Argonne Leadership Computing Facility, which is a DOE Office of Science User Facility supported under Contract No. DE-AC02-06CH11357. This research also used resources of the Oak Ridge Leadership Computing Facility, which is a DOE Office of Science User Facility supported under Contract No. DE-AC05-00OR22725. This research used resources of the National Energy Research Scientific Computing Center, a DOE Office of Science User Facility supported by the Office of Science of the US Department of Energy under Contract No. DE-AC02-05CH11231.

---

[1] N. F. Mott, Proc. Phys. Soc. Sec. A **62**, 416 (1949).

[2] G. A. Sawatzky and J. W. Allen, Phys. Rev. Lett. **53**, 2339 (1984).

[3] A. Fujimori and F. Minami, Phys. Rev. B **30**, 957 (1984).

[4] Z. Szotek, W. M. Temmerman, and H. Winter, Phys. Rev. B **47**, 4029 (1993).

[5] S. Massidda, A. Continenza, M. Posternak, and A. Baldereschi, Phys. Rev. B **55**, 13494 (1997).

[6] J. Zaanen, G. A. Sawatzky, and J. W. Allen, Phys. Rev. Lett. **55**, 418 (1985).

[7] T. M. Schuler, D. L. Ederer, S. Itza-Ortiz, G. T. Woods, T. A. Callcott, and J. C. Woicik, Phys. Rev. B **71**, 115113 (2005).

[8] H. Sato, T. Minani, S. Takata, and T. Yamada, Thin Solid Films **236**, 27 (1993).

[9] J. Kunes, V. I. Anisimov, A. V. Lukoyanov, and D. Vollhardt, Phys. Rev. B **75**, 165115 (2007).

[10] S. Nandy, U. N. Maiti, C. K. Ghosh, and K. K. Chattopadhyay, J. Phys.: Condens. Matter **21**, 115804 (2009).

[11] M. Yang, Z. Shi, J. Feng, H. Pu, G. Li, J. Zhou, and Q. Zhang, Thin Solid Films **519**, 3021 (2011).

[12] E. Antolini, Mater. Chem. Phys. **82**, 937 (2003).

[13] P. Kuiper, G. Kruizinga, J. Ghijsen, G. A. Sawatzky, and H. Verweij, Phys. Rev. Lett. **62**, 221 (1989).

[14] J. van Elp, H. Eskes, P. Kuiper, and G. A. Sawatzky, Phys. Rev. B **45**, 1612 (1992).

[15] I. J. Pickering, G. N. George, J. T. Lewandowski, and A. J. Jacobson, J. Am. Chem. Soc. **115**, 4137 (1993).

[16] S. Lany, J. Osorio-Guillén, and A. Zunger, Phys. Rev. B **75**, 241203(R) (2007).

[17] W.-L. Jang, Y.-M. Lu, W.-S. Hwang, and W.-C. Chen, J. Eur. Ceram. Soc. **30**, 503 (2010).

[18] H. Chen and J. H. Harding, Phys. Rev. B **85**, 115127 (2012).

[19] K. Matsubara, S. Huang, M. Iwamoto, and W. Pan, Nanoscale **6**, 688 (2014).

[20] T. Dutta, P. Gupta, A. Gupta, and J. Narayan, J. Appl. Phys. **108**, 083715 (2010).

[21] J. Osorio-Guillén, S. Lany, and A. Zunger, AIP Conf. Proc. **1199**, 128 (2010).

[22] M. Yang, H. Pu, Q. Zhou, and Q. Zhang, Thin Solid Films **520**, 5884 (2012).

[23] Y. R. Danny, K. Lee, C. Park, S. K. Oh, H. J. Kang, D.-S. Yang, and S. Seo, Thin Solid Films **591**, 255 (2015).

[24] L. Shulenburger and T. R. Mattsson, Phys. Rev. B **88**, 245117 (2013).

[25] H. Shin, S. Kang, J. Koo, H. Lee, J. Kim, and Y. Kwon, J. Chem. Phys. **140**, 114702 (2014).

[26] A. Benali, L. Shulenburger, N. A. Romero, J. Kim, and O. A. von Lilienfeld, J. Chem. Theory Comput. **10**, 3417 (2014).

[27] P. Ganesh, J. Kim, C. Park, M. Yoon, F. A. Reboredo, and P. R. C. Kent, J. Chem. Theory Comput. **10**, 5318 (2014).

[28] L. Shulenburger, A. D. Baczewski, Z. Zhu, J. Guan, and D. Tománek, Nano Lett. **15**, 8170 (2015).

[29] Y. Luo, A. Benali, L. Shulenburger, J. T. Krogel, O. Heinonen, and P. R. C. Kent, New J. Phys. **18**, 113049 (2016).

[30] A. Benali, L. Shulenburger, J. T. Krogel, X. Zhong, P. R. C. Kent, and O. Heinonen, Phys. Chem. Chem. Phys. **18**, 18323 (2016).

[31] K. Foyevtsova, J. T. Krogel, J. Kim, P. R. C. Kent, E. Dagotto, and F. A. Reboredo, Phys. Rev. X **4**, 031003 (2014).

[32] L. K. Wagner and P. Abbamonte, Phys. Rev. B **90**, 125129 (2014).

[33] M. Dubeck, L. Mitas, and P. Jureka, Chem. Rev. **116**, 5188 (2016).

[34] N. Devaux, M. Casula, F. Decremps, and S. Sorella, Phys. Rev. B **91**, 081101 (2015).

[35] E. Mostaani, M. Szyniszewski, C. H. Price, R. Maezono, M. Danovich, R. J. Hunt, N. D. Drummond, and V. I. Fal'ko, Phys. Rev. B **96**, 075431 (2017).

[36] J. Yu, L. K. Wagner, and E. Ertekin, Phys. Rev. B **95**, 075209 (2017).

[37] J. A. Santana, J. T. Krogel, J. Kim, P. R. C. Kent, and F. A. Reboredo, J. Chem. Phys. **142**, 164705 (2015).

[38] J. A. Santana, J. T. Krogel, P. R. C. Kent, and F. A. Reboredo, J. Chem. Phys. **144**, 174707 (2016).

[39] I. Kylänpää, J. Balachandran, P. Ganesh, O. Heinonen, P. R. C. Kent, and J. T. Krogel, Phys. Rev. Mater. **1**, 065408 (2017).

[40] W. M. C. Foulkes, L. Mitas, R. J. Needs, and G. Rajagopal, Rev. Mod. Phys. **73**, 33 (2001).

[41] P. J. Reynolds, D. M. Ceperley, B. J. Alder, and W. A. Lester, J. Chem. Phys. **77**, 5593 (1982).

[42] J. Kim, K. P. Esler, J. Mcminis, M. A. Morales, B. K. Clark, L. Shulenburger, and D. M. Ceperley, J. Phys.: Conf. Ser. **402**, 012008 (2012).

[43] P. Giannozzi, S. Baroni, N. Bonini, M. Calandra, R. Car, C. Cavazzoni, D. Ceresoli, G. L. Chiarotti, M. Cococcioni, I. Dabo, A. D. Corso, S. de Gironcoli, S. Fabris, G. Fratesi, R. Gebauer, U. Gerstmann, C. Gougoussis, A. Kokalj, M. Lazzeri, L. M. Samos, N. Mazari, F. Mauri, R. Mazzarello, S. Paolini, A. Pasquarello, L. Paulatto, C. Sbraccia, S. Scandolo, G. Sclauzero, A. P. Seitsonen, A. Smogunov, P. Umari, and R. M. Wentzcovitch, J. Phys.: Condens. Matter **21**, 395502 (2009).

[44] J. P. Perdew and A. Zunger, Phys. Rev. B **23**, 5048 (1981).

[45] J. P. Perdew, K. Burke, and M. Ernzerhof, Phys. Rev. Lett. **77**, 3865 (1996).

[46] V. I. Anisimov, J. Zaanen, and O. K. Andersen, Phys. Rev. B **44**, 943 (1991).

[47] S. L. Dudarev, G. A. Botton, S. Y. Savrasov, C. J. Humphreys, and A. P. Sutton, Phys. Rev. B **57**, 1505 (1998).

[48] A. I. Liechtenstein, V. I. Anisimov, and J. Zaanen, Phys. Rev. B **52**, 5467(R) (1995).

[49] Opium package; http://opium.sourceforge.net.

[50] C. Mitra, J. T. Krogel, J. A. Santana, and F. A. Reboredo, J. Chem. Phys. **143**, 164710 (2015).

[51] See Supplemental Material at http://link.aps.org/supplemental/10.1103/PhysRevMaterials.1.073603 for more information on (1) validation of the accuracy of the K pseudopotential, (2) input and output files for FHI-aims, pwscf, and VASP calculations, (3)

the DMC optical gap of NiO with variational parameter *U*, and (4) the DMC spin densities.

[52] C. Lin, F. H. Zong, and D. M. Ceperley, Phys. Rev. E **64**, 016702 (2001).

[53] N. D. Drummond, R. J. Needs, A. Sorouri, and W. M. C. Foulkes, Phys. Rev. B **78**, 125106 (2008).

[54] S. Chiesa, D. M. Ceperley, R. M. Martin, and M. Holzmann, Phys. Rev. Lett. **97**, 076404 (2006).

[55] V. Blum, R. Gehrke, F. Hanke, P. Havu, V. Havu, X. Ren, K. Reuter, and M. Scheffler, Comput. Phys. Commun. **228**, 2175 (2009).

[56] P. E. Blöchl, Phys. Rev. B **50**, 17953 (1994).

[57] G. Kresse and D. Joubert, Phys. Rev. B **59**, 1758 (1999).

[58] G. Kresse and J. Hafner, Phys. Rev. B **49**, 14251 (1994).

[59] G. Kresse and J. Furthmüller, Comput. Mater. Sci. **6**, 15 (1996).

[60] H. J. Kulik, M. Cococcioni, D. A. Scherlis, and N. Marzari, Phys. Rev. Lett. **97**, 103001 (2006).

[61] J. A. Schiller, L. K. Wagner, and E. Ertekin, Phys. Rev. B **92**, 235209 (2015).

[62] J. Kolorenč, S. Hu, and L. Mitas, Phys. Rev. B **82**, 115108 (2010).

[63] D. R. Lide, *CRC Handbook of Chemistry and Physics*, 75th ed. (CRC Press, Boca Raton, FL, 1995).

[64] In Ref. [50], all production calculations were performed with local spin density approximation orbitals generated with fixed (insulatorlike) occupations during the SCF cycle. In preproduction calculations aimed at exploring the effect of a Hubbard *U* parameter on the nodal surface, the *U* parameter was erroneously set to 0 in the trial wave functions due to a software error. As a consequence, Ref. [50] incorrectly concluded that a *U* parameter has no measurable effect on the DMC total energy. The plain local spin density approximation was then selected and used consistently for all production calculations in that work.

[65] J. Kolorenč and L. Mitas, Rep. Prog. Phys. **74**, 026502 (2011).

[66] J. Yu, L. K. Wagner, and E. Ertekin, J. Chem. Phys. **143**, 224707 (2015).

[67] Reference [50] also calculated the quasiparticle indirect gap as the difference between the electron affinity and the ionization potential.

[68] Y. Yan, S. B. Zhang, and S. T. Pantelides, Phys. Rev. Lett. **86**, 5723 (2001).

[69] Y. Wang, R. Zhang, J. Li, L. Li, and S. Lin, Nanoscale Res. Lett. **9**, 46 (2014).

[70] S. Hüfner, F. Hulliger, J. Osterwalder, and T. Riesterer, Soild State Commun. **50**, 83 (1984).

[71] S. Hüfner and T. Riesterer, Phys. Rev. B **33**, 7267 (1986).

[72] J. Zaanen, G. A. Sawatzky, and J. W. Allen, J. Magn. Magn. Mater. **54-57**, 607 (1986).

[73] M. G. Medvedev, I. S. Bushmarinov, J. Sun, J. P. Perdew, and K. A. Lyssenko, Science **355**, 49 (2017).

[74] W.-B. Zhang, N. Yu, W.-Y. Yu, and B.-Y. Tang, Eur. Phys. J. B **64**, 153 (2008).

[75] J. Yu, K. M. Rosso, and S. M. Bruemmer, J. Phys. Chem. C **116**, 1948 (2012).

[76] A. Wasserman, J. Nafziger, K. Jiang, M.-C. Kim, E. Sim, and K. Burke, Annu. Rev. Phys. Chem. **68**, 555 (2017).

[77] S. Song, M.-C. Kim, E. Sim, A. Benali, O. Heinonen, and K. Burke, arXiv:1708.08425 [cond-mat].

[78] A. Droghetti, D. Alfè, and S. Sanvito, Phys. Rev. B **87**, 205114 (2013).